

3D-Printed Omnidirectional Luneburg Lens Retroreflectors for Low-Cost mm-Wave Positioning

Ryan A. Bahr, Ajibayo O. Adeyeye, Samantha Van Rijs, and Manos M. Tentzeris
 School of Electrical and Computer Engineering, Georgia Institute of Technology
 Georgia Institute of Technology
 Atlanta, GA 30332

Abstract— This paper proposes the use of low-cost 3D printed Luneburg lenses as retroreflectors in microwave applications. Luneburg lenses have previously been associated with unnecessarily costly structures due to the stepped gradient index using multilayered spherical shells. Within the context of additive manufacturing, the gradient dielectric profile utilized in a Luneburg lens reduces the cost of fabrication, enabling a reevaluation of the use of the device in modern applications. In this paper, additively manufactured Luneburg lens retroreflector topologies which have a near omnidirectional response across the azimuthal plane are demonstrated, which aim to function in a similar fashion to traditional low-cost infrared-based retroreflectors spheres used in high resolution positioning systems, with the added ability to work in low-visibility conditions or in infrared-saturated environments, such as a sunny day. The retroreflective Luneburg lens radar cross section is measured and demonstrate basic positioning principles.

Keywords—Luneburg Lens, retroreflectors, 3D Printed, Gradient Index materials, additive manufacturing, positioning, localization

I. INTRODUCTION

Currently our society is in a transitional state where unmanned aircraft systems (UAS) have transformed from an expensive hobby, as well as military use, to becoming both a consumer level device and opening new industrial applications including package delivery and 3D photographic mapping. The U.S. Department of Transportation's Federal Aviation Administration (FAA) put in a request for public input for remote identification in December 2019 due to the growing number of drones, with nearly 1.5 million registered drones. The small form-factor and limited power supplies of UAS impose additional considerations, and the sheer number of drones expected in the future raises concern of flooding compatibility with existing communication technologies such as Automatic Dependent Surveillance – Broadcast (ADS-B). Swarm robotics have demonstrated impressive possibilities, ranging from firework-alternative light shows, large scale tree planting operations, and search and rescue missions. The scalability of the number drones in a swarm has a variety of factors, including physical factors such as aerodynamics, as well as the positioning systems utilized. For the last decade, the most extreme high-speed coordinated drones demonstrations utilize infrared camera positioning systems that enable high precision and frame rates that enable rapid feedback and the ability to distinguish and locate multiple robots with sub-mm precision. A variety of systems exist, but one of the most popular optoelectronic measurement systems (OMS) is the Vicon motion capture

platform, enabling update rates exceeding 100 hertz and with an average accuracy of approximately 2 mm, though sub-millimeter is possible [1]. The platform utilizes multiple spheres with retroreflective coatings which are illuminated with infrared light sources co-located on cameras lenses, with as many as 6 or more high speed cameras located near the ceiling edge of a room. Utilizing the spatial pattern of several reflective spheres on a robot enables identification information in addition to the positioning. While these systems are often seen as the gold standard for motion capture, they have a limited volume, with the largest known measurement setup consisting of an area of 824 m², relied on operating at night to avoid infrared interference from sunlight, while still having missing frames of data due to the line-of-sight (LOS) requirements [2]. Electromagnetic measurement systems (EMS) motion capture have benefits including non-line of sight (NLOS), but often have low accuracy or require active components. Through wall measurements utilizing corner retroreflective structures have been demonstrated [3]. This leads to a motivation of creating a microwave equivalent system that can act in a similar manner to the Vicon OMS with the benefits of EMS, enabling a reduction in the LOS requirements, operation in outdoor environments and increased range. The first step moving forward on that would be the creation of equivalent retroreflectors for RF applications.

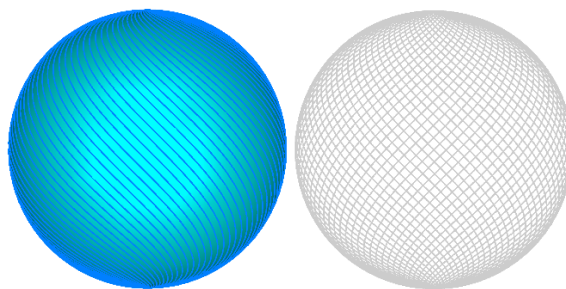


Fig. 1. The gradient index Luneburg sphere (left) visible demonstrating the surface of the polarizer and (right) how the polarizer changes orientation as it wraps around the sphere is apparent when the Luneburg lens dielectric core is hidden from view.

While Luneburg lenses have existed since the 1940s, they were originally fabricated utilizing multiple discrete spherical shells, with the increasing number of shells benefiting performance but often increasing costs proportionally as well [4]. Recently, Luneburg lenses have demonstrated as becoming cost-effective due to additive manufacturing, where earlier work demonstrated X-band Luneburg lenses, where the authors have further demonstrated the economic potential with a startup founded on the work focused on fabricating Luneburg lenses for

next generation automotive radar and 5G applications [5]. In most Luneburg lens applications, the lens is utilized for its gain enhancement, similar to a dielectric lens, with the additional benefit that the spherical symmetry enables infinite focal points across the surface of the sphere, enabling high gain beam steering by utilizing multiple feed points on the surface of the lens.

Luneburg lenses can also be utilized in various retroreflective topologies, which enable a high radar cross section (RCS), desirable to increase the visibility of an object under interrogation from an emission source. They have seen use in nautical applications to increase the visibility of ships at sea, as well as the Ball Lens In The Space (BLITS) satellite, used for submillimeter ranging accuracy over an 800 km distance. In the BLITS application, half of the sphere is coated with a reflective surface, which offers a 180 degrees of coverage. In order to achieve a more omnidirectional response, there exists multiple topologies of varying complexity, including a ring around the equator, or slightly offset, which offers an omnidirectional response across the plane of the ring with some aperture blockage [6]. While spheres are often utilized, there exist both flat Luneburg lenses and Luneburg lens metamaterials, both which can be realized with various manufacturing processes including traditional printed circuit boards (PCB) [7].

This paper presents 3D-printed omnidirectional Luneburg lens retroreflectors using additive manufacturing for positioning applications in the mm-Wave regime. While an additively manufactured Luneburg lens retroreflector has been demonstrated, the topology was similar to the BLITS [8], with limited coverage due to the hemisphere copper reflector. In this paper a topology explored is based off the heliosphere antenna, in which a slanted linear polarizer covers the surface of the sphere and appears to have a different polarization depending on if the incident wave is entering or exiting the Luneburg lens reflector [9, 10]. This design demonstrated in Fig. 1 aims to explore the use of additively manufactured omnidirectional Luneburg reflector topologies that can enable extremely low-cost retroreflective structures for various applications, including road markers for self-driving cars, small spheres utilized for passive tracking of people, or objects with an EMS-based motion capture system. This will provide a foundational exploration for increasingly smart spheres, where the integration of spherical conformal metasurfaces and antennas enable identification of the spheres for sensing and synthetic aperture radar applications [11, 12].

II. THEORY

With the rapid growth of mm-wave radar and phased array systems becoming a widespread consumer product, retroreflective structures have demonstrated renewed attention in recent years as a method of increasing radar cross section (RCS), enabling increases in signal-to-noise ratios (SNR), and thus various parameters including range and accuracy in both passive and active systems. There has been demonstrations of the use of modulated retroreflector (MRR) in the mm-wave band which has recently demonstrated improved performance for long range sensor applications [13, 14]. Various retroreflective structures exist, one of the most used is the rounded corner cube

reflector (CCR) which enables a simple construction of three rounded orthogonal metallic plates. These structures have been used in many structures, the most well-known is the lunar laser ranging experiment, where optical CCRs are used to precisely determine the distance of the moon.

$$\sigma_{\text{Round Corner Cube Reflector}} = \frac{15.6\pi L^4}{3\lambda^2} \quad (1)$$

CCRs have been well characterized, a key feature that has enabled their use as a reference tool alongside metallic spheres for RCS measurements. With a max RCS at boresight, the calculation of the RCS is demonstrated in (1), where L the length of a side and λ is the wavelength. The pattern of the corner reflector drops by an order of magnitude approximately 30 degrees from bore-sight [12]. In order to increase the RCS response across a larger angle, several CCRs are placed with rotational symmetry to create a wider angle of response. An alternative approach is to utilize a spherical lens reflector (SLR), a sphere with a metal backing, which demonstrates an increase response in oblique angles where the RCS drops an order of magnitude a 60 degrees off boresight, approximately double angular coverage of a CCR. A Luneburg lens reflector with a simple metal backing further improves upon the SLR by further improving the acceptance angle [8].

A. Luneburg Lens Retroreflectors

A Luneburg lens utilizes a gradient material to create, in its most common form, a radially symmetric lens that has infinite focal points on the surface of the sphere. It has been demonstrated that the Luneburg lens retroreflector (LLR) maximum RCS approaches that of circular plate as seen in (2), where r is the radius of the plate and λ the wavelength [7]. Many variations of the lens exist that alter the dielectric profile to adjust the focal point, but to achieve the focal point on the surface of the sphere, a dielectric profile based on (3) is utilized, where r is the radial position and R , the radius of the sphere.

$$\sigma_{\text{Circular Plate}} = \frac{4\pi^3 r^4}{\lambda^2} \quad (2)$$

$$\epsilon = 2 - \left(\frac{r}{R}\right)^2 \quad (3)$$

Achieving gradient materials can be done through several methods, ranging from a discrete amount of layers of different materials or a gradual mixture of materials during fabrication. Previous publications suggest that a stepped index Luneburg lens should contain at least 11 layers in order to demonstrate significant improvement over a simple spherical lens (consisting of a single dielectric of $n = 2$) [4]. For fabrication purposes, the GRADIENT INDEX (GRIN) material is created utilizing a simple cubic metamaterial (SCM) structure as seen in Fig. 2, which consists of a structural beam width b , and a lattice constant a between cells [15]. The width determines the volume ratio of the dielectric vs air, and utilizing the Maxwell-Garnett's effective medium theory, an estimation of the effective dielectric permittivity can be determined by iteratively adjusting the width of the lattice. The fabrication method must be considered, as the minimum feature size in combination with the permittivity of

the material deposited will create the range of achievable effective permittivity by the lattice structure.

$$\epsilon_{eff} = \epsilon_m \frac{2\delta_i(\epsilon_i - \epsilon_m) + \epsilon_i + 2\epsilon_m}{2\epsilon_m + \epsilon_i - \delta_i(\epsilon_i - \epsilon_m)} \quad (4)$$

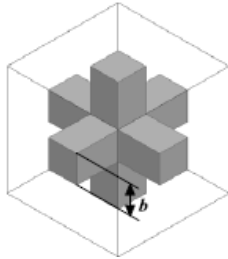


Fig. 2. Simple Cubic Metamaterial lattice structure [15].

B. Modeling of 3D Luneburg Lens

For simulation purposes, the Luneburg lens is modeled as a continuously gradient dielectric sphere without loss. This is achieved through the spherically spatially varying dielectric materials parameters with CST Microwave Studio in the time domain solver. The simple cubic lattice structure for the Luneburg lens is achieved through a custom Visual Basic macro which varies the width of the lattice structure based Maxwell Garnett's effective medium theory (4) where δ_i is the volume fraction of the inclusion (in this case, polymer), ϵ_i is the permittivity of the inclusion, and ϵ_m is the permittivity of the matrix (in this case, air). The effective medium theory is utilized in conjunction with the Luneburg profile in (3) to create the gradient index structure. While the effective medium theory offers an estimation that can be considered sufficient, a more accurate model may be considered where each inclusion ratio is iteratively simulated with periodic boundary conditions to extract the effective material properties while considering the coupling effects of nearby lattice cells. An octant of a sphere is constructed, and then mirrored in its entirety three times to create the sphere. The lattice constant a determines the operational upper cutoff frequency of the SCM, where a must be 3 times larger than the operational frequency to prevent Bragg diffraction and appear as a homogenous and isotropic effective medium [16].

C. Slanted Polarizers

The heliosphere debuted an interesting concept by utilizing slanted wire grid linear polarizers on a sphere. When looking at the surface of the sphere, it becomes apparent that the conformal wrapping of the polarizer onto the sphere causes the polarizer to rotate its polarization on the opposite end of the incident wave [9]. This does pose limitations on the interrogating system of either using slanted polarization, or compromise with circular polarization and a 6 dB polarization mismatch loss for additional orientation independent operation. In Fig. 1, the polarizer is compared with an opaque and transparent sphere to make this apparent. There are some trade-offs in this design. While a wire grid polarizer has a high acceptance angle, which is ideal for spherical operation, the wire grid polarizer can not stay parallel across the entire doubly curved surface with respect to the aperture of the

incident wave, which is apparent in Fig. 3. Utilizing infinitely thin wires for simulation within CST demonstrated an improved RCS that approaches towards the circular plate as the number of polarizers increases, but always demonstrates a noticeable aperture blockage due the polarizers that are non-parallel with respect to the incident wave. In order to realize the polarizer with traditional fabrication, a minimal feature size must be defined for the width of the polarizer, which leads to a noticeable amount of aperture blockage specifically at the poles of the sphere. While the wire grid polarizers do not operate under the same polarizer-reversing response at the poles, an incident wave can still have a significant RCS response due to retroreflectivity, just with a lower magnitude than the response along the azimuth.

In order to reliably fabricate the polarizers on a Form3 3D printer, the polarizers have a width of 0.771 mm and thickness of 0.800 mm, with a total of 72 polarizers that has a 1-to-1 ratio of coverage vs uncovered surface area, as shown in Fig. 3. While reducing the number of polarizers would increase the exposed surface area, the amount of energy reflected decreases as well. In this paper, a 50 mm LLR is demonstrated, which would have an ideal RCS of -3.15 dBsm for an ideal circular plate as defined in (2). With the polarizers designed as mentioned, with a lossless spatially varying dielectric and perfectly electrical conductors, the simulated RCS is -6.32 dBsm at 30 GHz, a 3.17 dB difference from the ideal scenario of a circular plate.

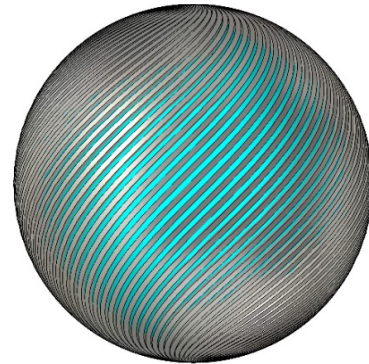


Fig. 3. Luneburg lens with spherically conformal finite-width slanted polarizer.

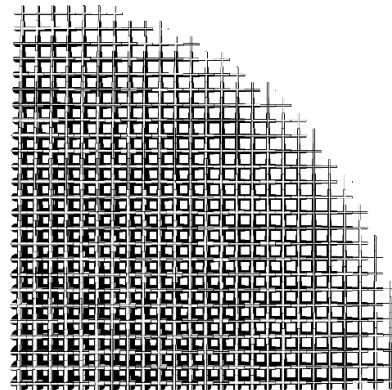


Fig. 4. 3D model generated with the visual basic macro of an octant of the Luneburg lens model, demonstrating the varying b as a function of the radius.

D. 3D Printing of Luneburg Lenses

Additive manufacturing offers a wide range of properties that are still being explored in various fields, and has seen rapid adoption in the last ten years. Certain structures that were cost prohibitive actually excel with the fabrication technology, including the lattice structures used in conjunction with effective mediums for GRIN materials.

One of the cheapest 3D printers is a fused deposition modeling (FDM) printer, which heats plastic filaments past the glass transition temperature (t_g) and deposits it from a nozzle, typically of 400 μm diameter and achieving 50 μm layers. More extreme 3D printing technologies can achieve various minimum feature sizes, some as low as 100 nm utilizing 2-photon polymerization. Often the higher resolution techniques utilizing lithography processes with photopolymers tend to have an order of magnitude increase in dielectric loss, as well as material costs. FDM materials, while lower resolution offer the ability to print relatively pure, lower loss, thermoplastic materials. For example, at the time photopolymers may cost approximately \$150 per liter with a $\tan\delta$ of 0.02-0.04, while FDM thermoplastics often cost around \$15/kg with a $\tan\delta$ of 0.008 or less [17]. Nonetheless, the lattice structure offers additional cost benefits vs traditional solid step-index Luneburg lenses by reducing the total volumetric material used approximately by 65%, based upon the volume of the modeled lattice structure in this work. Natural colored (ABS) is utilized, a relative low loss material often used in the automotive industry due to various mechanical properties, including temperature tolerances. While the accuracy of a print can be affected by a variety of factors, including printing speed, so long as the volume of material extruded is accurate, effective medium theory enables visible defects to have limited effects on performance.

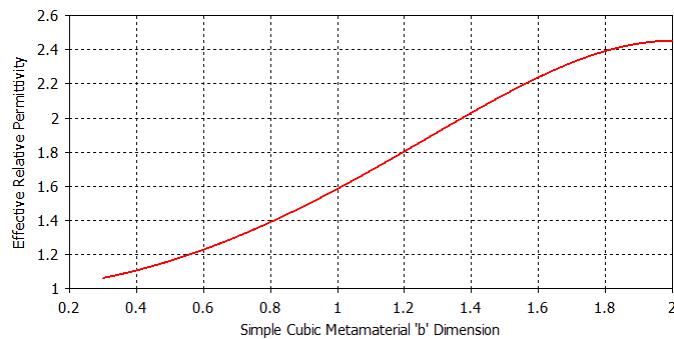


Fig. 5. Effective medium theory dielectric permittivity range based off minimum feature size of FDM 3D printing.

The properties of ABS were characterized at e-band (60-90 GHz) using a (NRW), with a permittivity of $\epsilon_r = 2.45$ and a $\tan\delta = 0.007$. Utilizing the effective medium theory, the table of possible effective permittivity values are calculated and demonstrated in Fig. 3, enabling a range between 1.06 and 2.45 based on the minimal feature size of 300 μm , shown in Fig. 5. While the varying dielectric material model does enable dielectric losses, the effective loss tangent due to the effective medium theory is not account for. The loss tangent has a significant impact on the RCS performance of solid dielectric lens, though the effective medium will improve the performance of dielectric materials. The 50 mm diameter Luneburg lens are

fabricated by printing half a lattice sphere and assembling the two halves together with a minimal amount of adhesive, with the two halves shown in Fig. 6. The lattice constant was 2.5 mm, with an expected operational frequency of up to 40 GHz due to Bragg's diffractions as discussed in [9].



Fig. 6. Luneburg lens halves of 50 mm diameter with a 2.5 mm lattice constant FDM printed with ABS plastic.

The spherical linear polarizers model in Fig. 3 were printed with a Form3 printer with FormLabs High Temperature resin, with the dimensions previously mentioned of 0.771 mm width and 0.80 mm thickness, which had a negligible effect in simulations. The polarizer had to be fabricated in two halves to encase the Luneburg lens, and due to the delicate nature of the structure, had to be printed with support material which must be carefully removed after printing. In Fig. 7, the support material is shown before removal, and after removal the polarizer is coated with two layers of LPKF ProConduct Paste, with a 30 minute cure at 150 $^{\circ}\text{C}$ between each layer. Imperfections due to the unsupported lengths of the polarizer resulting some variation in gap size, as well as some surface imperfections due to removal of the support material are visible, and may be mitigated by utilizing a printing process such as material jetting, where a sacrificial wax support structure is printed.



Fig. 7. 3D printed slanted polarizer shell on Form3 with FormLabs High Temperature material (left) before metallization and (right) after metallization with LPKF ProConduct Paste.

E. Bandwidth Considerations.

There are several considerations for operational bandwidth, which can have an effect of the design in this paper. While the system can have a wideband performance which offers improved localization, there are specific properties that contribute towards a low and high frequency cutoff. As mentioned earlier, the lattice spacing can lead to Bragg's diffraction due to constructive interference, and acts as a high frequency limit typically dictated by the resolution of

the 3D printing technology. The wire grid polarizers also have a high frequency limit, so long as the spacing between polarizers is electrically small. Finally, the size of the sphere comes into consideration as well, where for the best response the sphere should operate beyond the Rayleigh regime, where the circumference divided by wavelength is less than 1 and preferably in the optical regime where that same ratio is greater than 10. The wide bandwidth of the LLR enables the use of the structure in frequency modulated continuous wave (FMCW) radar systems, often employed in automotive radar, where the bandwidth directly correlates towards the resolution of the radar.

III. MEASUREMENTS

Several measurements were done to verify the operation of the LLR and their relevance towards positioning applications. Two horn antennas (A-INFOMW LB-180400-20-C-KF) were set up in a TX/RX configuration with an Anritsu MS46522B VNA set to measure from 18 GHz to 40 GHz. Both interrogating horn antennas are slanted 45° for polarization purposes. The 50 mm LLR was fully rotated in 1° increments, with the two port response saved. While Fig.8 shows the LLR in the lab environment on a supporting cardboard box, a foam disc was later utilized. A measurement of the background was removed from the response of the LLR. Finally, a measurement of a 12-inch conductive sphere was used as a reference RCS for de-embedding of the estimated RCS of the LLR. The s-parameter results are then passed through an inverse fast Fourier transform (IFFT) to bring to the time domain, where time gating is utilized to isolate the return of the sphere and LLR, before returning the results back to the frequency domain, based on the recommendations by Anritsu in [18]. Once the response of the 12 inch sphere is processed, with a calculated RCS of -11.37 dBsm based on (5), the sphere measurement can be used as a reference to calculate the response of the LLR based upon the difference of the sphere and LLR response, as seen in (6). The measured response of the sphere was -71.24 dB, and the response of the 50 mm LLR was -70.02 dB, which corresponds to a measured RCS of -10.15 dBsm for the LLR at 30 GHz.

$$\sigma_{Sphere} = \pi r^2 \quad (5)$$

$$RCS_{tgt} (dBsm) = RCS_{std} (dB) - RCS_{tgt} (dB) \quad (6)$$

For the measurement of distance location of Luneburg lenses, a reference measurement is first made at a known distance to set as a reference plane, used to calibrate any delays in the measurement path. Utilizing an IFFT, the response is plotted against the distance using time domain reflectometry (TDR) with respect to the horn antenna. After the pattern is measured, a preliminary investigation of the LLR behind a 178 mm thick cardboard box was measured as well, with the measurement layout shown in Fig. 9.

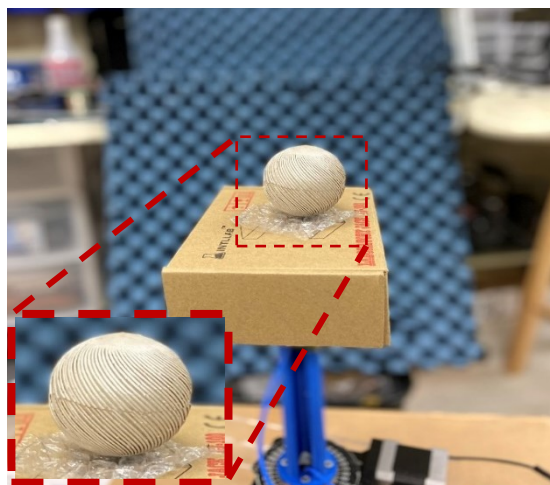


Fig. 8. RCS measurement setup in a lab environment. The LLR is attached to a stepper motor and interrogated slanted horn antennas.

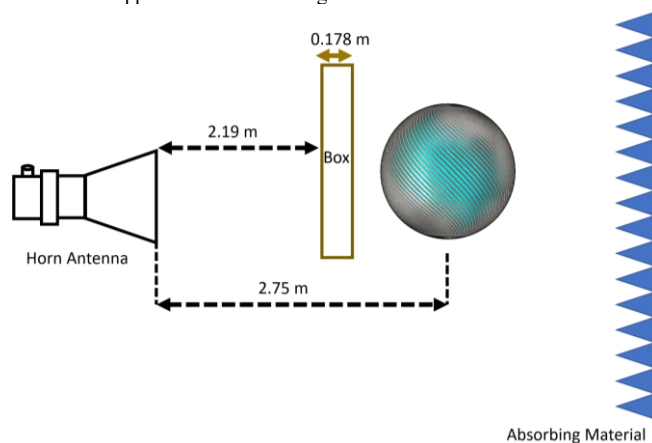


Fig. 9. Measurement setup. A 0.178 m thick cardboard box was positioned at 2.19 m distance from interrogating horn antennas.

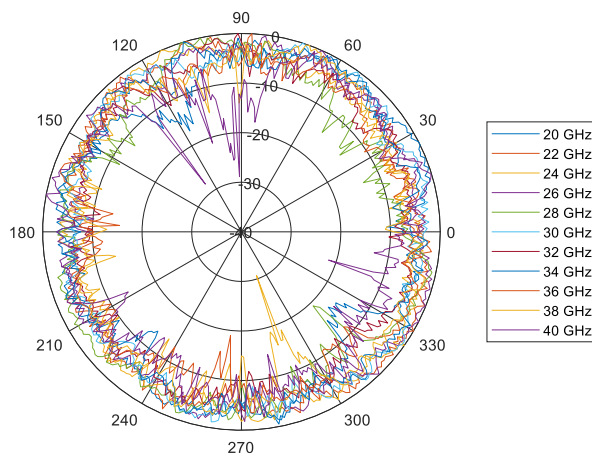


Fig. 10. Normalized RCS (dB) measurements from 20 GHz to 40 GHz in 2 GHz increments.

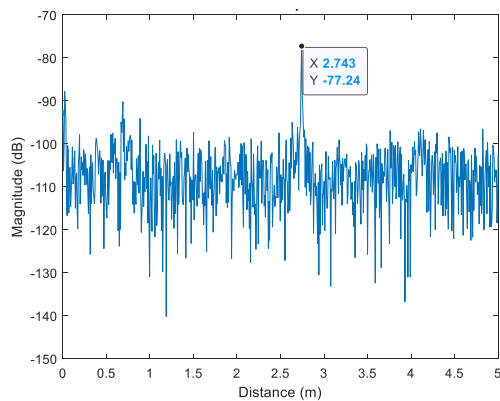


Fig. 11. Time domain measurements of LLR.

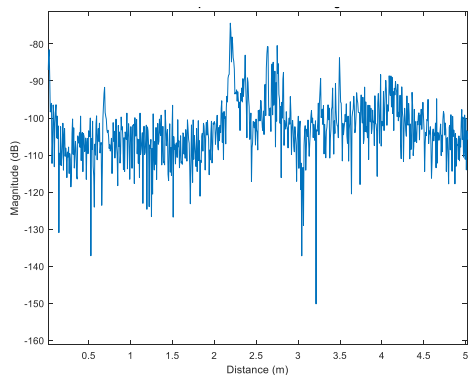


Fig. 12. Measurement with 178 mm cardboard box blocking line of sight, where the LLR is located at 2.75 m and the box occupies the space between 2.19 m and 2.368 m.

IV. RESULTS

The normalized RCS pattern of the 50 mm sphere can be seen in Fig. 10. The RCS stays relatively constant for RCS measurements across the 18 to 40 GHz measurement frequency with a few noticeable dips. These dips are possibly attributed with either the wire polarizer grid cut in half for assembly, or imperfections in the wire grid polarizer due to the strain from removal of support material. The RCS of -10.15 dBsm at 30 GHz differs from the -6.327 dBsm lossless simulation model mentioned early by 3.823 dB. A full wave simulation of the SCM lattice structure demonstrates less than 0.3 dB variance from the spatially varying dielectric model available within CST, which may be attributed to meshing variances between the two large structures. Incorporating ABS's property of $\tan\delta = 0.007$ contributes an additional 1.4 dB of dielectric loss within the SCM lattice simulation. This suggests that 2.4 dB of loss may possibly result imperfections from the assembly process of two halves, or possibly due to over- or under- extrusion with the FDM printer. The TDR response demonstrates the response of the Luneburg lens reflector, and a brief investigation shows a response behind closed 178 mm thick large cardboard box, with the layout shown in Fig. 9 and the measured results shown in Fig. 12. While the hollow cardboard box had a thickness of 0.178 m, the surface area normal to the incident wave had a width and height of approximately 0.400 m by 0.700 m, relatively large and contributes a significant response. While the result demonstrates that the LLR is still visible, additional

methods that improve isolating the response from the environment, such as backscatter modulation, can further improve the performance of the system. Improved fabrication processes where the lattice constant is further reduced, resulting in both an increased upper cutoff frequency and an increased RCS, will be likely be necessary for e-band automotive radar.

V. CONCLUSIONS

The authors have demonstrated the first known results of a 3D printed Luneburg lens omnidirectional retroreflector. Results demonstrate the RCS properties of low-cost Luneburg Lens reflectors across mm-wave bands, demonstrating a clear response and omnidirectional pattern across the azimuth plane. Improvements upon the topology can be realized as multi-material printers that enable direct printing of conductors allow the integration of the polarizers without additional assembly, creating a more exact design from simulation to fabrication. With the renewed interest in Luneburg lenses, there is still a wide amount of future work we expect to see including: additional characterization of additively manufactured novel Luneburg Lens topologies, integrated radomes, the frequency and angular response due to Bragg reflections. With ever improving 3D printers, we expect to see demonstrate these topologies achieve cutoff frequencies above the 70 GHz band relevant to automotive radar in the near future, as well as enabling improved NLOS tracking when used with modulation techniques. The ability to create low cost, light weight retroreflectors with a broad angle of response will enable RCS enhancement that is useful in a variety of applications, such as drone detection, novel motion capturing systems, and outdoor swarm robotics, where passive reflective structures and compatibility with various radar bands enable rapid adoption.

REFERENCES

- [1] Merriaux, Pierre & Dupuis, Yohan & Boutheau, Rémi & Vasseur, Pascal & Savatier, Xavier. (2017). A Study of Vicon System Positioning Performance. *Sensors*. 17. 1591. 10.3390/s17071591.
- [2] Eline van der Kruk & Marco M. Reijne (2018) Accuracy of human motion capture systems for sport applications; state-of-the-art review, *European Journal of Sport Science*, 18:6, 806-819
- [3] Amin, Moeness & Ahmad, Fauzia. (2014). Chapter 17. Through-the-Wall Radar Imaging: Theory and Applications. Academic Press Library in Signal Processing. 2.D.
- [4] Jain, Sidharath & Abdel-Mageed, Mohamed & Mittra, Raj. (2013). Flat-Lens Design Using Field Transformation and Its Comparison With Those Based on Transformation Optics and Ray Optics. *IEEE Antennas and Wireless Propagation Letters*. 12.
- [5] M. Liang, W. Ng, K. Chang, K. Gbele, M. E. Gehm and H. Xin, "A 3-D Luneburg Lens Antenna Fabricated by Polymer Jetting Rapid Prototyping," in *IEEE Transactions on Antennas and Propagation*, vol. 62, no. 4, pp. 1799-1807, April 2014, doi: 10.1109/TAP.2013.2297165.
- [6] H. E. Schrank, "Spherical radar reflectors with high-gain omnidirectional response," in *Proceedings of the IEEE*, vol. 53, no. 8, pp. 1117-1118, Aug. 1965, doi: 10.1109/PROC.1965.4112.
- [7] C. Pfeiffer and A. Grbic, "A Printed, Broadband Luneburg Lens Antenna," in *IEEE Transactions on Antennas and Propagation*, vol. 58, no. 9, pp. 3055-3059, Sept. 2010, doi: 10.1109/TAP.2010.2052582.
- [8] J. C. Deroba, K. D. Sobczak, A. Good, Z. Larimore and M. Mirotznik, "Additively Manufactured Luneburg Retroreflector," in *IEEE Aerospace and Electronic Systems Magazine*, vol. 34, no. 11, pp. 20-24, 1 Nov. 2019, doi: 10.1109/MAES.2019.2944050.
- [9] J. Flaherty and E. Kadak, "Early warning radar antennas," 1958 IRE International Convention Record, New York, NY, USA, 1958, pp. 158-165, doi: 10.1109/IRECON.1958.1150709.

- [10] Diamond, M., 1966. MICROWAVE REFLECTOR. 3251061.
- [11] W. Su, S. Wang, R. Bahr and M. M. Tentzeris, "Smart Floating Balls: 3D Printed Spherical Antennas and Sensors for Water Quality Monitoring," *2018 IEEE/MTT-S International Microwave Symposium - IMS*, Philadelphia, PA, 2018, pp. 55-58, doi: 10.1109/MWSYM.2018.8439350.
- [12] Williams, Richard & Gatesman, Andrew & Goyette, Thomas & Giles, Robert. (2014). Radar cross section measurements of frequency selective terahertz retroreflectors. *Proceedings of SPIE - The International Society for Optical Engineering*. 9102.
- [13] Henry, J. G. D. Hester, H. Aubert, P. Pons and M. M. Tentzeris, "Long range wireless interrogation of passive humidity sensors using Van-Atta cross-polarization effect and 3D beam scanning analysis," *2017 IEEE MTT-S International Microwave Symposium (IMS)*, Honolulu, HI, 2017, pp. 816-819.
- [14] Alhassoun, M. A. Varner and G. D. Durgin, "Design and evaluation of a multi-modulation retrodirective RFID tag," *2018 IEEE International Conference on RFID (RFID)*, Orlando, FL, 2018, pp. 1-8. Spherical reflector
- [15] Y. Li, L. Ge, M. Chen, Z. Zhang, Z. Li and J. Wang, "Multibeam 3-D-Printed Luneburg Lens Fed by Magnetolectric Dipole Antennas for Millimeter-Wave MIMO Applications," in *IEEE Transactions on Antennas and Propagation*, vol. 67, no. 5, pp. 2923-2933, May 2019, doi: 10.1109/TAP.2019.2899013.
- [16] Zhao, Y.-Y., Zhang, Y.-L., Zheng, M.-L., Dong, X.-Z., Duan, X.-M. and Zhao, Z.-S. (2016), Three-dimensional Luneburg lens at optical frequencies. *Laser & Photonics Reviews*, 10: 665-672
- [17] P. I. Deffenbaugh, R. C. Rumpf and K. H. Church, "Broadband Microwave Frequency Characterization of 3-D Printed Materials," in *IEEE Transactions on Components, Packaging and Manufacturing Technology*, vol. 3, no. 12, pp. 2147-2155, Dec. 2013.
- [18] P. I. Deffenbaugh, T. M. Weller and K. H. Church, "Fabrication and Microwave Characterization of 3-D Printed Transmission Lines," in *IEEE Microwave and Wireless Components Letters*, vol. 25, no. 12, pp. 823-825, Dec. 2015.
- [19] M. Grace, "Measurement of Radar Cross Section Using the "VNA Master" Handheld VNA: Application Note," Anritsu2011